Nano Research 2016, 9(5): 1358–1365
DOI 10.1007/s12274-016-1031-z
Research Article

ISSN 1998-0124
CN 11-5974/O4

Controllable synthesis of triangular $Ni(HCO_3)_2$ nanosheets for supercapacitor

Xiaoxian Zang, Ziyang Dai, Jing Guo, Qiuchun Dong, Jun Yang, Wei Huang (✉), and Xiaochen Dong (✉)

Key Laboratory of Flexible Electronics (KLOFE) & Institute of Advanced Materials (IAM), Jiangsu National Synergetic Innovation Center for Advanced Materials (SICAM), Nanjing Tech University (NanjingTech), Nanjing 211816, China

Received: 3 December 2015
Revised: 19 January 2016
Accepted: 25 January 2016

KEYWORDS
nickel bicarbonate,
nanosheets,
anodes,
supercapacitor

ABSTRACT

Triangular $Ni(HCO_3)_2$ nanosheets were synthesized via a template-free solvothermal method. The phase transition and formation mechanism were explored systematically. Further investigation indicated that the reaction time and pH have significant effects on the morphology and size distribution of the triangular $Ni(HCO_3)_2$ nanosheets. More interestingly, the resulting product had an ultra-thin structure and high specific surface area, which can effectively accelerate the charge transport during charge–discharge processes. As a result, the triangular $Ni(HCO_3)_2$ nanosheets not only exhibited high specific capacitance (1,797 $F \cdot g^{-1}$ at 5 $A \cdot g^{-1}$ and 1,060 $F \cdot g^{-1}$ at 50 $A \cdot g^{-1}$), but also showed excellent cycling stability with a high current density (~80% capacitance retention after 5,000 cycles at the current density of 20 $A \cdot g^{-1}$).

1 Introduction

With the increasing depletion of fossil fuels and aggravated environmental pollution, sustainable and renewable energy storage and conversion are urgently needed. Supercapacitors [1] are gaining extensive interest because of their high power density (>10 $kW \cdot kg^{-1}$), fast recharge capacity (within seconds), and long cycle life (>10^5 cycles) [2, 3]. However, the wide practical usage of supercapacitors is prevented by the limited energy density (~5–20 $kW \cdot kg^{-1}$) [4]. The development of novel electrode materials that can afford high energy density and good stability performance is becoming one of the key tasks [5]. Among a multitude of electrode materials, nickel composites show promise owing to their excellent intrinsic properties and excellent electrochemical performance. For example, nickel-based $Ni(OH)_2$ [6–8] and NiO [9, 10] have been fabricated and applied as supercapacitor electrode materials owing to their high theoretical specific capacitance and low cost. Also, metal sulfides and even metal phosphides, such as NiS [11, 12] and NiP [13, 14], have received considerable attention because of their high capacitance. However, the poor electrical conductivity of these kinds of materials seriously limits the performance of the supercapacitors [15, 16]. To address this problem, novel nanostructures, especially two-dimensional materials with large specific surface

Address correspondence to Xiaochen Dong, iamxcdong@njtech.edu.cn; Wei Huang, iamwhuang@njtech.edu.cn

areas, have aroused extensive attention on account of their higher charge transfer rates during the electrochemical process [17].

Recently, $Ni(HCO_3)_2$ nanosheets, a new type of two-dimensional nanomaterial, have attracted the attention of researchers interested in supercapacitor electrode materials. Sun et al. [18] synthesized $Ni(HCO_3)_2$ nanoparticles and graphene composites and employed them as supercapacitor electrode materials. In addition, a high specific capacitance was achieved in a 6 M potassium hydroxide (KOH) solution, which is superior to those of most nickel-based electrode materials [19, 20]. Yan et al. prepared sphere-like $Ni(HCO_3)_2$ nanoparticles, and their supercapacitor performance was explored in detail [21]. However, obtaining $Ni(HCO_3)_2$ nanosheets with controlled morphology is still a huge challenge.

Here, a facile template-free solvothermal route was proposed for the synthesis of triangular $Ni(HCO_3)_2$ nanosheets. The morphology and size distribution of the triangular $Ni(HCO_3)_2$ nanosheets can be controlled easily by adjusting the reaction time. When employed as electrode materials in supercapacitors, the unique nanostructure is beneficial to the reduction of the effective diffusion paths and results in faster charge transport. Its specific capacitance can reach 1,797 $F \cdot g^{-1}$ at 5 $A \cdot g^{-1}$ and 1,060 $F \cdot g^{-1}$ at 50 $A \cdot g^{-1}$. More importantly, the triangular $Ni(HCO_3)_2$ supercapacitor exhibits excellent cycling stability (~80% capacitance retention after 5,000 cycles at 20 $A \cdot g^{-1}$).

2 Experimental

2.1 Preparation of triangular $Ni(HCO_3)_2$ nanosheets

In this study, triangular $Ni(HCO_3)_2$ nanosheets were synthesized via a facile template-free solvothermal method. Typically, 2 mmol of nickel nitrate hexahydrate ($Ni(NO_3)_2 \cdot 6H_2O$) and 8 mmol of urea ($CO(NH_2)_2$) were dissolved in deionized (DI) water. Then, ethylene glycol (volume ratio between DI water and ethylene glycol of 1:7) was added to form a homogeneous solution. Afterwards, the resultant mixture was transferred into a 50 mL Teflon-lined stainless steel autoclave and heated at 140 ℃ for 12 h in an oven. Finally, the product was collected and washed with DI water and ethyl alcohol several times, then dried at 80 ℃ for 6 h. For the purpose of comparison, products were synthesized with different reaction time using the same process.

2.2 Characterization

X-ray diffraction (XRD, Bruker D8 Advance) was applied to analyze the structures of the samples. The morphologies of the samples were examined by field-emission scanning electron microscopy (FESEM, Zeiss Ultra-55), transmission electron microscopy (TEM, Hitachi, HT7700 and JEOL, 2010), and atomic force microscopy (AFM, Bruker Dimension Icon). The specific surface area of the sample was measured using nitrogen adsorption–desorption isotherms with a Micromeritics ASAP 2020 surface area and porosity analyzer. The pore size distribution was evaluated using the adsorption branch of the isotherm based on the Barrett–Joyner–Halenda (BJH) model. The pH value of the reaction solution was determined with a pH apparatus (Mettler Toledo S220 Seven Compact).

2.3 Electrochemical measurements

A conventional three-electrode system (CHI 760D, CH Instruments Inc., China) was employed with a saturated Ag/AgCl electrode as a reference electrode, a platinum plate as a counter electrode, and active materials as a working electrode. The working electrodes were fabricated by coating Ni foil with a mixture containing 70 wt.% active materials, 20 wt.% conductive agent (acetylene black), and 10 wt.% polyvinylidene fluoride (PVDF). The loading mass of the active material was approximately 4 $mg \cdot cm^{-2}$. KOH aqueous solution (3.0 M) was used as the electrolyte. The electrochemical performance was measured using cyclic voltammetry (CV), galvanostatic charge–discharge tests, and electrochemical impedance spectroscopy (EIS) measurements (1–100,000 Hz).

3 Results and discussion

In this study, triangular $Ni(HCO_3)_2$ nanosheets were synthesized via a template-free solvothermal method. During the synthesis process, nickel ions and negative ions (OH^- or HCO_3^-) can participate in a phase-transfer reaction and form a nickel-based two-dimensional

nanomaterial. To understand the structural and morphological changing process of the $Ni(HCO_3)_2$ nanosheet, a series of samples were synthesized with different reaction time (3, 6, 9, and 12 h). Figure 1 shows the XRD patterns of the four samples. As shown in Fig. 1(a), for the sample synthesized in 3 h, three main diffraction peaks can be clearly identified at around 11.3°, 33.4°, and 60.0°, corresponding to the single crystalline phase of $Ni(OH)_2$ (JCPDS No. 38-0715) [22, 23]. With prolonged reaction time, $Ni(HCO_3)_2$ diffraction peaks indexed to the standard powder diffraction file (PDF) card (JCPDS No. 15-0782, $a = b = c$ = 8.383 Å) [24, 25] appeared stronger in the XRD patterns (Fig. 1(b)). Finally, after increasing the reaction time to 12 h, the diffraction peaks of $Ni(OH)_2$ disappeared completely. The absence of $Ni(OH)_2$ diffraction peaks and the rise of $Ni(HCO_3)_2$ diffraction peaks indicated that $Ni(OH)_2$ had completely changed to the $Ni(HCO_3)_2$ phase in the 12 h reaction.

Figure 2 shows the TEM images of the four samples synthesized at different reaction time. As shown in Fig. 2(a), the $Ni(OH)_2$ nanosheets obtained at 3 h show an ultra-thin two-dimensional structure with some wrinkles uniformly distributed on its surface. For the case of the sample with the 6 h reaction time, some small and regular triangular $Ni(HCO_3)_2$ nanosheets appeared and were deposited onto the surface of the previously formed $Ni(OH)_2$ nanosheets. The length of the triangular nanosheets was approximately 60 nm. Upon increasing the reaction time further to 9 h, more $Ni(OH)_2$ nanosheets gradually turned into triangular-shaped $Ni(HCO_3)_2$ nanosheets. However, the size of the $Ni(OH)_2$ nanosheets significantly decreased. The TEM image in Fig. 2(d) indicates that the $Ni(OH)_2$ nanosheets completely transformed into uniform triangular-shaped $Ni(HCO_3)_2$ nanosheets when the 12 h reaction was finished. The transition process of the samples can also be confirmed by the FESEM images (Fig. S1 in the Electronic Supplementary Material (ESM)). Furthermore, AFM measurement indicated that the average thickness of the triangular $Ni(HCO_3)_2$ nanosheets was ~14 nm (Fig. S2 in the ESM). High-resolution TEM (HRTEM) measurement indicated that the distinct fringe spacing was ~0.59 nm, which corresponds very well to the (110) crystal plane of $Ni(HCO_3)_2$ (Fig. 3(a)). Moreover, the distinguishable

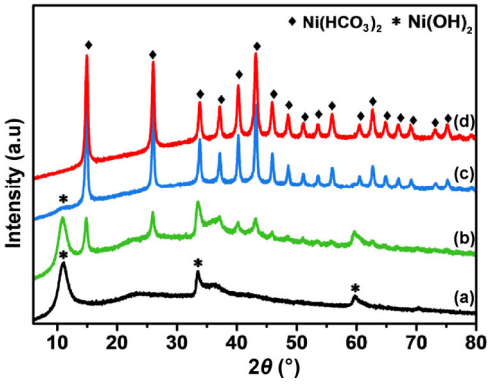

Figure 1 XRD patterns of the samples synthesized at different reaction time: (a) 3 h, (b) 6 h, (c) 9 h, and (d) 12 h.

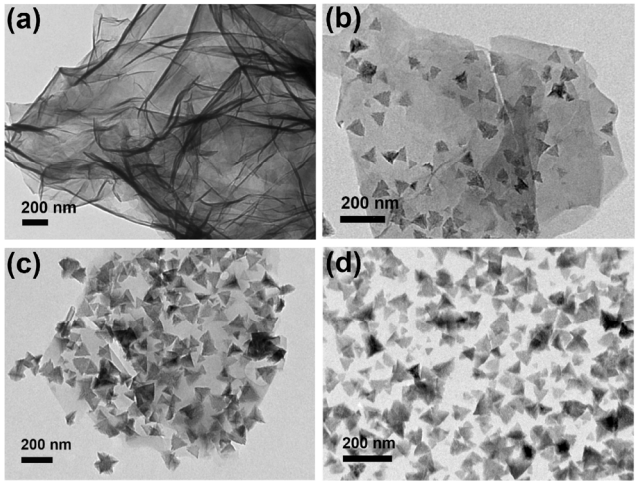

Figure 2 TEM images of the samples synthesized at different reaction time: (a) 3 h, (b) 6 h, (c) 9 h, and (d) 12 h.

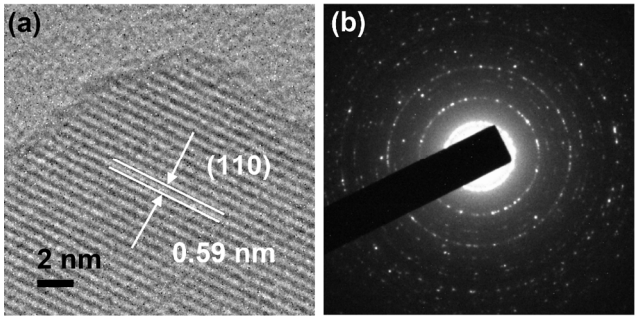

Figure 3 (a) HRTEM image and (b) SAED image of triangular $Ni(HCO_3)_2$ nanosheets.

ring-like feature in the selected area electron diffraction (SAED) pattern can be an indication of the polycrystalline structure of the $Ni(HCO_3)_2$ nanosheets (Fig. 3(b)).

Based on the XRD and TEM measurements, a possible formation mechanism of the triangular $Ni(HCO_3)_2$ nanosheets is proposed and illustrated in Scheme 1.

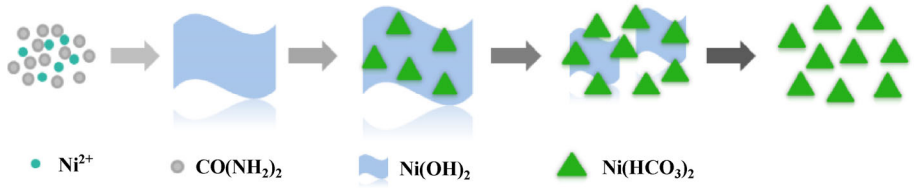

Scheme 1 Possible formation mechanism of triangular $Ni(HCO_3)_2$ nanosheets.

During the heating process, the generated OH^- ions produced by the decomposition of urea react with Ni^{2+} and form $Ni(OH)_2$ nanosheets in a short time (3 h). Afterwards, the later-produced HCO_3^-, owing to the more difficult hydrolysis process of CO_2 than that of NH_3, reacts with the $Ni(OH)_2$ and produces $Ni(HCO_3)_2$ nanosheets. With the increase in reaction time, the HCO_3^- causes $Ni(OH)_2$ to completely transform into $Ni(HCO_3)_2$. Here, the main reactions of the urea homogeneous solvothermal method for the synthesis of $Ni(HCO_3)_2$ are as follows

Urea hydrolysis

$$CO(NH_2)_2 + 3H_2O \rightarrow 2NH_3{\cdot}H_2O + CO_2 \quad (1)$$

Ammonia ionization

$$NH_3{\cdot}H_2O \rightarrow NH_4^+ + OH^- \quad (2)$$

Precipitation reaction of $Ni(OH)_2$

$$Ni^{2+} + 2OH^- \rightarrow Ni(OH)_2 \quad (3)$$

Carbon dioxide ionization

$$CO_2 + H_2O \rightarrow HCO_3^- + H^+ \quad (4)$$

Precipitation reaction of $Ni(HCO_3)_2$

$$Ni(OH)_2 + 2HCO_3^- \rightarrow Ni(HCO_3)_2 + 2OH^- \quad (5)$$

It should be noted that the pH values of the reaction solution increased from 8.75 to 9.08 with the increase in reaction time, which further confirms the phase transition from $Ni(OH)_2$ to $Ni(HCO_3)_2$.

Figure 4(a) shows the nitrogen adsorption–desorption curve of the triangular $Ni(HCO_3)_2$ nanosheets. It can be found that the isotherms are type III isotherms with a hysteresis loop at a relative pressure P/P_0 from 0.7 to 1.0, indicating that the triangular $Ni(HCO_3)_2$ nanosheets have a mesoporous structure. The calculated Brunauer–Emmett–Teller (BET) specific surface area of $Ni(HCO_3)_2$ nanosheets is approximately 97.1 $m^2{\cdot}g^{-1}$. Figure 4(b) shows the pore size distribution calculated from the desorption data using the BJH model. The average pore size of $Ni(HCO_3)_2$ nanosheets is approximately 12 nm. The obtained mesoporous structure (2 to 20 nm) can promote the transport and diffusion of electrolyte ions during the charge–discharge process, which also results in enhanced electrochemical efficiency [26, 27].

The electrochemical performance of the as-prepared samples was evaluated in a conventional three-electrode system with a 3.0 M KOH electrolyte. Figure 5(a) shows the typical CV curve of the $Ni(OH)_2$ and $Ni(HCO_3)_2$ nanosheets measured at a scan rate of 20 $mV{\cdot}s^{-1}$. In both of the CV curves, a pair of well-defined redox peaks can be observed clearly, which are

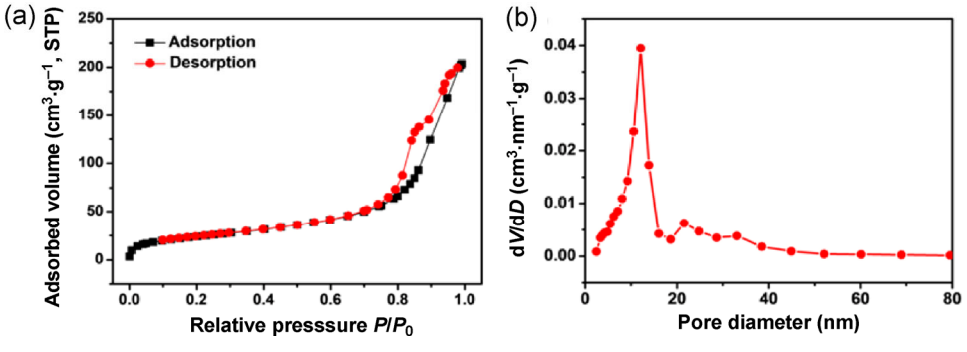

Figure 4 (a) Nitrogen adsorption–desorption isotherm and (b) pore-size-distribution curve of triangular $Ni(HCO_3)_2$ nanosheets.

distinguishable from those of electric double-layer capacitors and indicate the presence of a reversible Faradaic reaction and pseudocapacitive behavior [28, 29]. The redox reactions during the charge/discharge of $Ni(OH)_2$ and $Ni(HCO_3)_2$ electrodes can be described by the following equations [18, 21, 30]

$$Ni(OH)_2 + OH^- \leftrightarrows NiOOH + H_2O + e^- \quad (6)$$

$$Ni(HCO_3)_2 + 3OH^- \leftrightarrows NiOOH + 2HCO_3^- + H_2O + e^- \quad (7)$$

Moreover, the integral area of $Ni(HCO_3)_2$ is larger than that of $Ni(OH)_2$, indicating that the specific capacitance of $Ni(HCO_3)_2$ is higher than that of $Ni(OH)_2$. Figure 5(b) shows the CV curves of the triangular $Ni(HCO_3)_2$ nanosheets at different scan rates ranging from 2.0 to 20 $mV \cdot s^{-1}$. With the increase in scan rate, the peak currents increase correspondingly, indicating ideal capacitive behavior and fast charge–discharge performance for electrochemical energy storage [31, 32].

Galvanostatic charge–discharge (GCD) curves of the triangular $Ni(HCO_3)_2$ nanosheets at various current densities are shown in Fig. 5(c). According to the GCD curves, a high specific capacitance (1,797 $F \cdot g^{-1}$) can be achieved at a current density of 5 $A \cdot g^{-1}$. Even at a high current density (50 $A \cdot g^{-1}$), the specific capacitance of $Ni(HCO_3)_2$ nanosheets can reach approximately 1,060 $F \cdot g^{-1}$, which is much higher than that of $Ni(OH)_2$ nanosheets (Fig. S3(a) in the ESM). Furthermore, the slight decrease in capacitance with the increase in the charge/discharge current (Fig. 5(d)) indicates that the $Ni(HCO_3)_2$ nanosheets allow the redox reaction to take place rapidly at high current densities. The high electrochemical performance of the $Ni(HCO_3)_2$ nanosheets may be attributed to their unique nanostructure. The mesoporous structured $Ni(HCO_3)_2$ nanosheets can provide more electrochemical active sites and consequently increase the efficiency of electrochemical reactions.

Figure 6(a) shows the cycle performances of $Ni(OH)_2$ and $Ni(HCO_3)_2$ nanosheet electrodes at a current density of 20 $A \cdot g^{-1}$. It can be seen that the capacitance retention of $Ni(OH)_2$ nanosheets was close to 50% after 5,000 cycles. In contrast, there was only a decrease of approximately 20% in the capacitance for the $Ni(HCO_3)_2$ nanosheet electrode after 5,000 cycles. This shows that $Ni(HCO_3)_2$ nanosheets have excellent long-term cycling stability even at a high current density. Figure 6(b) displays the Nyquist plots of the $Ni(HCO_3)_2$ nanosheet electrode before and after 5,000 charge–discharge cycles. It can be found that

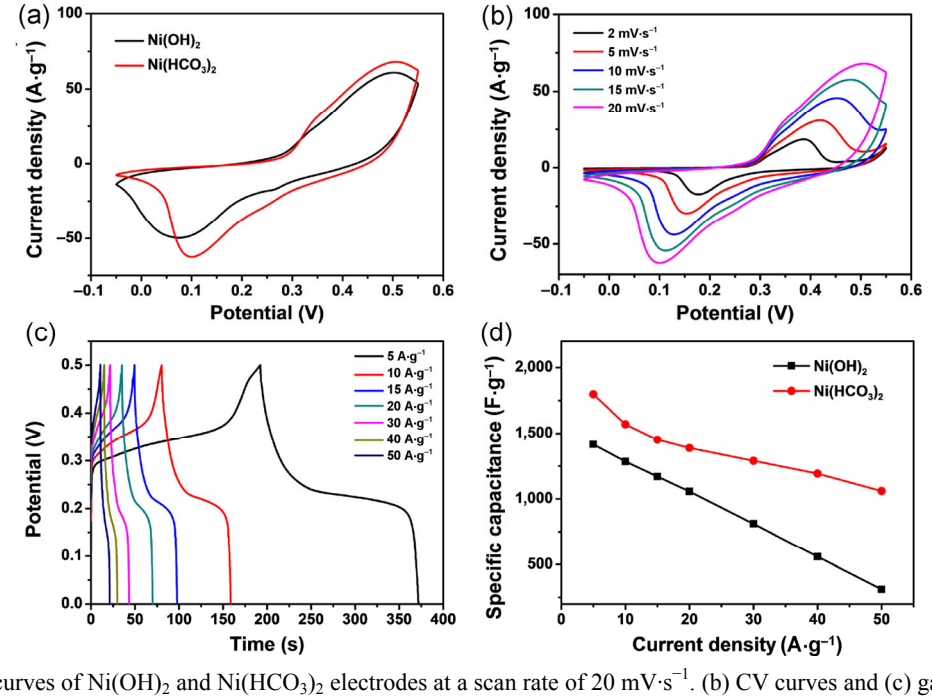

Figure 5 (a) CV curves of $Ni(OH)_2$ and $Ni(HCO_3)_2$ electrodes at a scan rate of 20 $mV \cdot s^{-1}$. (b) CV curves and (c) galvanostatic charge–discharge curves of $Ni(HCO_3)_2$ electrode. (d) Specific capacitance of $Ni(OH)_2$ and $Ni(HCO_3)_2$ electrodes measured as a function of current density.

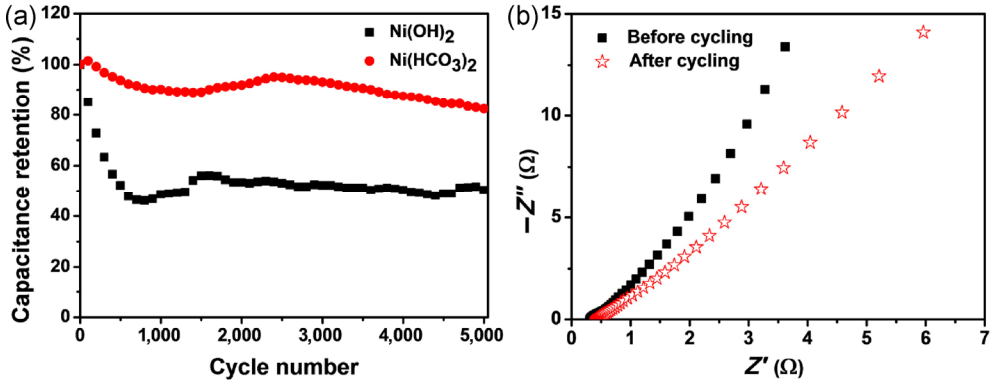

Figure 6 (a) Cycling stability of $Ni(OH)_2$ and $Ni(HCO_3)_2$ electrodes measured at a current density of 20 $A \cdot g^{-1}$. (b) Nyquist plots of the $Ni(HCO_3)_2$ electrode before and after 5,000 charge–discharge cycles at a current density of 20 $A \cdot g^{-1}$.

there was no obvious appearance of semicircles for the $Ni(HCO_3)_2$ nanosheet electrode, indicating that the charge-transfer resistance (*R*ct) of the electrode was low enough during the cycling test [33]. Furthermore, the sloping straight line at lower frequencies caused by the diffusion process reveals a typical capacitive behavior of the electrode [34]. After 5,000 cycles, the equivalent series resistance (ESR) shows a slight increase (~0.12 Ω) evaluated from the point intersecting with the real axis in the high-frequency range [35]. The slight changes in the Nyquist plots of the $Ni(HCO_3)_2$ electrode before and after the cycles further confirm the highly reversible redox reaction of the $Ni(HCO_3)_2$ electrode. EIS spectra of the $Ni(OH)_2$ and triangular $Ni(HCO_3)_2$ nanosheets (Fig. S3(b) in the ESM) show that the line of $Ni(HCO_3)_2$ in the low-frequency region is steeper than that of $Ni(OH)_2$, which facilitates the fast diffusion and migration of electrolyte ions [36]. Furthermore, the ESR of $Ni(HCO_3)_2$ in the high-frequency range is smaller than that of $Ni(OH)_2$. For comparison, the electrochemical performances of $Ni(HCO_3)_2$ electrodes reported recently are presented in Table S1 in the ESM. This suggests that the triangular $Ni(HCO_3)_2$ nanosheet electrode in this work shows higher specific capacitance and better cycle stability at a high current density.

4 Conclusions

In summary, a facile one-pot solvothermal method was applied to fabricate $Ni(HCO_3)_2$ nanosheets. By adjusting the reaction time, the triangular $Ni(HCO_3)_2$ nanosheets with a uniform triangular-shaped morphology, ultra-thin structure, and high specific surface area were successfully synthesized. The triangular $Ni(HCO_3)_2$ nanosheets exhibited a high specific capacitance (1,797 $F \cdot g^{-1}$ at 5 $A \cdot g^{-1}$ and 1,060 $F \cdot g^{-1}$ at 50 $A \cdot g^{-1}$) and excellent cycling stability (~80% capacitance retention after 5,000 cycles at 20 $A \cdot g^{-1}$). The high electrochemical performance indicates that $Ni(HCO_3)_2$ triangular nanosheets can potentially be used as energy storage materials.

Acknowledgements

The project was supported by the National Natural Science Foundation of China (Nos. 61525402 and 21275076), Jiangsu Provincial Funds for Distinguished Young Scholars (No. BK20130046), Program for New Century Excellent Talents in University (No. NCET-13-0853), QingLan Project, Synergetic Innovation Center for Organic Electronics and Information Displays, the Priority Academic Program Development of Jiangsu Higher Education Institutions (PAPD).

Electronic Supplementary Material: Supplementary material (SEM and AFM measurements, etc.) is available in the online version of this article at http://dx.doi.org/10.1007/s12274-016-1031-z.

References

[1] Wei, W. F.; Cui, X. W.; Chen, W. X.; Ivey, D. G. Manganese oxide-based materials as electrochemical supercapacitor

electrodes. *Chem. Soc. Rev.* **2011**, *40*, 1697–1721.

[2] Wang, G. P.; Zhang, L.; Zhang, J. J. A review of electrode materials for electrochemical supercapacitors. *Chem. Soc. Rev.* **2012**, *41*, 797–828.

[3] Balasingam, S. K.; Lee, J. S.; Jun, Y. Few-layered $MoSe_2$ nanosheets as an advanced electrode material for supercapacitors. *Dalton Trans.* **2015**, *44*, 15491–15498.

[4] Jiang, J.; Li, Y. Y.; Liu, J. P.; Huang, X. T.; Yuan, C. Z.; Lou, X. W. Recent advances in metal oxide-based electrode architecture design for electrochemical energy storage. *Adv. Mater.* **2012**, *24*, 5166–5180.

[5] Xu, Y. X.; Huang, X. Q.; Lin, Z. Y.; Zhong, X.; Huang, Y.; Duan, X. F. One-step strategy to graphene/$Ni(OH)_2$ composite hydrogels as advanced three-dimensional supercapacitor electrode materials. *Nano Res.* **2013**, *6*, 65–76.

[6] Wang, H. L.; Casalongue, H. S.; Liang, Y. Y.; Dai, H. J. $Ni(OH)_2$ nanoplates grown on graphene as advanced electrochemical pseudocapacitor materials. *J. Am. Chem. Soc.* **2010**, *132*, 7472–7477.

[7] Yan, J.; Fan, Z. J.; Sun, W.; Ning, G. Q.; Wei, T.; Zhang, Q.; Zhang, R. F.; Zhi, L. J.; Wei, F. Advanced asymmetric supercapacitors based on $Ni(OH)_2$/graphene and porous graphene electrodes with high energy density. *Adv. Funct. Mater.* **2012**, *22*, 2632–2641.

[8] Feng, G.; Kuang, Y.; Li, Y. J.; Sun, X. M. Three-dimensional porous superaerophobic nickel nanoflower electrodes for high-performance hydrazine oxidation. *Nano Res.* **2015**, *8*, 3365–3371.

[9] Huang, M. L.; Gu, C. D.; Ge, X.; Wang, X. L.; Tu, J. P. NiO nanoflakes grown on porous graphene frameworks as advanced electrochemical pseudocapacitor materials. *J. Power Sources* **2014**, *259*, 98–105.

[10] Bai, Y.; Du, M.; Chang, J.; Sun, J.; Gao, L. Supercapacitors with high capacitance based on reduced graphene oxide/carbon nanotubes/NiO composite electrodes. *J. Mater. Chem. A* **2014**, *2*, 3834–3840.

[11] Yang, J. Q.; Duan, X. C.; Qin, Q.; Zheng, W. J. Solvothermal synthesis of hierarchical flower-like β-NiS with excellent electrochemical performance for supercapacitors. *J. Mater. Chem. A* **2013**, *1*, 7880–7884.

[12] Yang, J. Q.; Duan, X. C.; Guo, W.; Li, D.; Zhang, H. L.; Zheng, W. J. Electrochemical performances investigation of NiS/rGO composite as electrode material for supercapacitors. *Nano Energy* **2014**, *5*, 74–81.

[13] Wang, D.; Kong, L.-B.; Liu, M.-C.; Zhang, W.-B.; Luo, Y.-C.; Kang, L. Amorphous Ni–P materials for high performance pseudocapacitors. *J. Power Sources* **2015**, *274*, 1107–1113.

[14] Du, W. M.; Wei, S. H.; Zhou, K. K.; Guo, J. J.; Pang, H.; Qian, X. F. One-step synthesis and graphene-modification to achieve nickel phosphide nanoparticles with electrochemical properties suitable for supercapacitors. *Mater. Res. Bull.* **2015**, *61*, 333–339.

[15] Zhang, J. T.; Liu, S.; Pan, G. L.; Li, G. R.; Gao, X. P. A 3D hierarchical porous α-$Ni(OH)_2$/graphite nanosheet composite as an electrode material for supercapacitors. *J. Mater. Chem. A* **2014**, *2*, 1524–1529.

[16] Yang, M. Y.; Cheng, H.; Gu, Y. Y.; Sun, Z. F.; Hu, J.; Cao, L. J.; Lv, F. C.; Li, M. C.; Wang, W. X.; Wang, Z. Y. et al. Facile electrodeposition of 3D concentration-gradient Ni–Co hydroxide nanostructures on nickel foam as high performance electrodes for asymmetric supercapacitors. *Nano Res.* **2015**, *8*, 2744–2754.

[17] Peng, X.; Peng, L. L.; Wu, C. Z.; Xie, Y. Two dimensional nanomaterials for flexible supercapacitors. *Chem. Soc. Rev.* **2014**, *43*, 3303–3323.

[18] Sun, J. F.; Li, Z. P.; Wang, J. Q.; Wang, Z. F.; Niu, L. Y.; Gong, P. W.; Liu, X. H.; Wang, H. G.; Yang, S. R. Solvothermal synthesis of $Ni(HCO_3)_2$/graphene composites toward supercapacitors and the faradiac redox mechanism in KOH solution. *J. Alloy. Compd.* **2013**, *581*, 217–222.

[19] Wu, M. S.; Lin, Y. P.; Lin, C. H.; Lee, J. T. Formation of nano-scaled crevices and spacers in NiO-attached graphene oxide nanosheets for supercapacitors. *J. Mater. Chem.* **2012**, *22*, 2442–2448.

[20] Zhu, X. J.; Dai, H. L.; Hu, J.; Ding, L.; Jiang, L. Reduced graphene oxide–nickel oxide composite as high performance electrode materials for supercapacitors. *J. Power Sources* **2012**, *203*, 243–249.

[21] Yan, Y. N.; Cheng, G.; Wang, P.; He, D. N.; Chen, R. Facile hydrothermal selective fabrication of $Ni(OH)_2$ and $Ni(HCO_3)_2$ nanoparticulates and their electrochemical performances. *RSC Adv.* **2014**, *4*, 49303–49307.

[22] Yang, S. B.; Wu, X. L.; Chen, C. L.; Dong, H. L.; Hu, W. P.; Wang, X. K. Spherical α-$Ni(OH)_2$ nanoarchitecture grown on graphene as advanced electrochemical pseudocapacitor materials. *Chem. Commun.* **2012**, *48*, 2773–2775.

[23] Chen, X.; Long, C. L.; Lin, C. P.; Wei, T.; Yan, J.; Jiang, L. L.; Fan, Z. J. Al and Co co-doped α-$Ni(OH)_2$/graphene hybrid materials with high electrochemical performances for supercapacitors. *Electrochim. Acta* **2014**, *137*, 352–358.

[24] Wu, X.; Pang, X. Y.; An, X.; Xie, X. M. Kinetics and mechanism of formation of benzoin ethyl ether from benzaldehyde and ethanol using heterogeneous $Ni(HCO_3)_2$ as catalyst. *Prog. React. Kinet. Mec.* **2014**, *39*, 299–307.

[25] Wu, X.; An, X.; Xie, X.-M. Preparation of $Ni(HCO_3)_2$ and its catalytic performance in synthesis of benzoin ethyl ether. *Trans. Nonferrous Met. Soc. China* **2014**, *24*, 1440–1445.

[26] Yan, J.; Sun, W.; Wei, T.; Zhang, Q.; Fan, Z. J.; Wei, F. Fabrication and electrochemical performances of hierarchical porous $Ni(OH)_2$ nanoflakes anchored on graphene sheets. *J. Mater. Chem.* **2012**, *22*, 11494–11502.

[27] Sennu, P.; Christy, M.; Aravindan, V.; Lee, Y. G.; Nahm, K. S.; Lee, Y. S. Two-dimensional mesoporous cobalt sulfide nanosheets as a superior anode for a Li-ion battery and a bifunctional electrocatalyst for the Li–O_2 system. *Chem. Mater.* **2015**, *27*, 5726–5735.

[28] Zhou, J.; Huang, Y.; Cao, X. H.; Ouyang, B.; Sun, W. P.; Tan, C. L.; Zhang, Y.; Ma, Q. L.; Liang, S. Q.; Yan, Q. Y.; Zhang, H. Two-dimensional $NiCo_2O_4$ nanosheet-coated three-dimensional graphene networks for high-rate, long-cycle-life supercapacitors. *Nanoscale* **2015**, *7*, 7035–7039.

[29] Hou, L. R.; Yuan, C. Z.; Li, D. K.; Yang, L.; Shen, L. F.; Zhang, F.; Zhang, X. G. Electrochemically induced transformation of NiS nanoparticles into $Ni(OH)_2$ in KOH aqueous solution toward electrochemical capacitors. *Electrochim. Acta* **2011**, *56*, 7454–7459.

[30] Xia, Q. X.; San Hui, K.; Hui, K. N.; Kim, S. D.; Lim, J. H.; Choi, S. Y.; Zhang, L. J.; Mane, R. S.; Yun, J. M.; Kim, K. H. Facile synthesis of manganese carbonate quantum dots/$Ni(HCO_3)_2$–$MnCO_3$ composites as advanced cathode materials for high energy density asymmetric supercapacitors. *J. Mater. Chem. A* **2015**, *3*, 22102–22117.

[31] Huo, H. H.; Zhao, Y. Q.; Xu, C. L. 3D Ni_3S_2 nanosheet arrays supported on Ni foam for high-performance supercapacitor and non-enzymatic glucose detection. *J. Mater. Chem. A* **2014**, *2*, 15111–15117.

[32] Lu, Z. Y.; Yang, Q.; Zhu, W.; Chang, Z.; Liu, J. F.; Sun, X. M.; Evans, D. G.; Duan, X. Hierarchical Co_3O_4@Ni–Co–O supercapacitor electrodes with ultrahigh specific capacitance per area. *Nano Res.* **2012**, *5*, 369–378.

[33] Chen, W.; Xia, C.; Alshareef, H. N. One-step electrodeposited nickel cobalt sulfide nanosheet arrays for high-performance asymmetric supercapacitors. *ACS Nano* **2014**, *8*, 9531–9541.

[34] Min, S. D.; Zhao, C. J.; Chen, G. R.; Qian, X. Z. One-pot hydrothermal synthesis of reduced graphene oxide/$Ni(OH)_2$ films on nickel foam for high performance supercapacitors. *Electrochim. Acta* **2014**, *115*, 155–164.

[35] Niu, L. Y.; Wang, J. Q.; Hong, W.; Sun, J. F.; Fan, Z. J.; Ye, X. Y.; Wang, H. G.; Yang, S. R. Solvothermal synthesis of Ni/reduced graphene oxide composites as electrode material for supercapacitors. *Electrochim. Acta* **2014**, *123*, 560–568.

[36] Sun, C. C.; Ma, M. Z.; Yang, J.; Zhang, Y. F.; Chen, P.; Huang, W.; Dong, X. C. Phase-controlled synthesis of α-NiS nanoparticles confined in carbon nanorods for high performance supercapacitors. *Sci. Rep.* **2014**, *4*, 7054.